ACS NANO

Cite This: ACS Nano 2019, 13, 505−514

www.acsnano.org

ARTICLE

Conformational Details of Quantum Dot-DNA Resolved by Förster Resonance Energy Transfer Lifetime Nanoruler

Jiajia Guo,[†,⊥] Xue Qiu,[†,⊥] Carlos Mingoes,[†] Jeffrey R. Deschamps,[‡] Kimihiro Susumu,[§,∥] Igor L. Medintz,[‡] and Niko Hildebrandt*[,†]

[†]NanoBioPhotonics, Institute for Integrative Biology of the Cell (I2BC), Université Paris-Saclay, Université Paris-Sud, CNRS, CEA, 91400 Orsay, France

[‡]Center for Bio/Molecular Science and Engineering, Code 6900 and [§]Optical Sciences Division, Code 5600, U.S. Naval Research Laboratory, Washington, D.C. 20375, United States

[∥]KeyW Corporation, Hanover, Maryland 21076, United States

Supporting Information

ABSTRACT: **DNA-nanoparticle conjugates are important tools in nanobiotechnology. Knowing the orientation, function, and length of DNA on nanoparticle surfaces at low nanomolar concentrations under physiological conditions is therefore of great interest. Here, we investigate the conformation of a 31 nucleotides (nt) long DNA attached to a semiconductor quantum dot (QD) *via* Förster resonance energy transfer (FRET) from Tb-DNA probes hybridized to different positions on the QD-DNA. Precise Tb-to-QD distance determination from 7 to 14 nm along 26 nt of the peptide-appended QD-DNA was realized by time-resolved FRET spectroscopy. The FRET nanoruler measured linear single-stranded (ssDNA) and double-stranded (dsDNA) extensions of ∼0.15 and ∼0.31 nm per base, reflecting the different conformations. Comparison with biomolecular modeling confirmed the denser conformation of ssDNA and a possibly more flexible orientation on the QD surface, whereas the dsDNA was fully extended with radial orientation. The temporally distinct photoluminescence decays of the different DNA-FRET configurations were used for prototypical DNA hybridization assays that demonstrated the large potential for extended temporal multiplexing. The extensive experimental and theoretical analysis of 11 different distances/configurations of the same QD-DNA conjugate provided important information on DNA conformation on nanoparticle surfaces and will be an important benchmark for the development and optimization of DNA-nanobiosensors.**

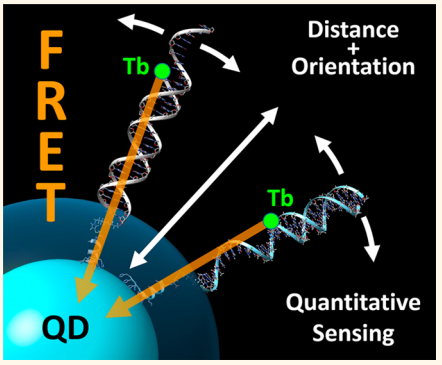

KEYWORDS: *FRET, quantum dots, nanoparticles, terbium, molecular ruler, conformation, sensing*

The development and application of DNA-nanoparticle conjugates for advanced chemical and biological sensing is a continuously growing field of research.[1−9] Understanding conformation and function of nucleic acids attached to nanosurfaces under physiological conditions is of paramount importance for the design of useful and versatile analytical tools with specific and sensitive target recognition. Semiconductor quantum dots (QDs) are among the most often applied nanoparticles for DNA-nanobiotechnology because their chemical and photophysical stability and outstanding fluorescence properties can be used for both investigating the DNA-nanosurface interaction and developing robust and sensitive biosensors.[10−17] In particular, the combination with Förster resonance energy transfer (FRET) or other nanometric energy or charge-transfer mechanisms allows for scrutinizing distance dependence and orientation of DNA-nanoparticle systems and for developing and optimizing DNA-hybridization biosensors with exceptional analytical properties.[18−23]

Arguably the most interesting aspect of DNA-nanotechnology is its simplicity of constructing single- or double-stranded structures out of only four types of bases, which allows for placing energy transfer donors and acceptors (molecules or nanoparticles) at defined distances with single nucleotide (nt) sensitivity (*e.g.*, ∼0.33 nm between two base pairs within a dsDNA).[24] Such flexibility in adapting donor−acceptor distances is useful for optimizing the energy transfer for each specific donor−acceptor pair with the aim of highest possible sensitivity. It can also be exploited to tune the photo-

Received: September 18, 2018
Accepted: December 3, 2018
Published: December 3, 2018

DOI: 10.1021/acsnano.8b07137
ACS Nano 2019, 13, 505−514

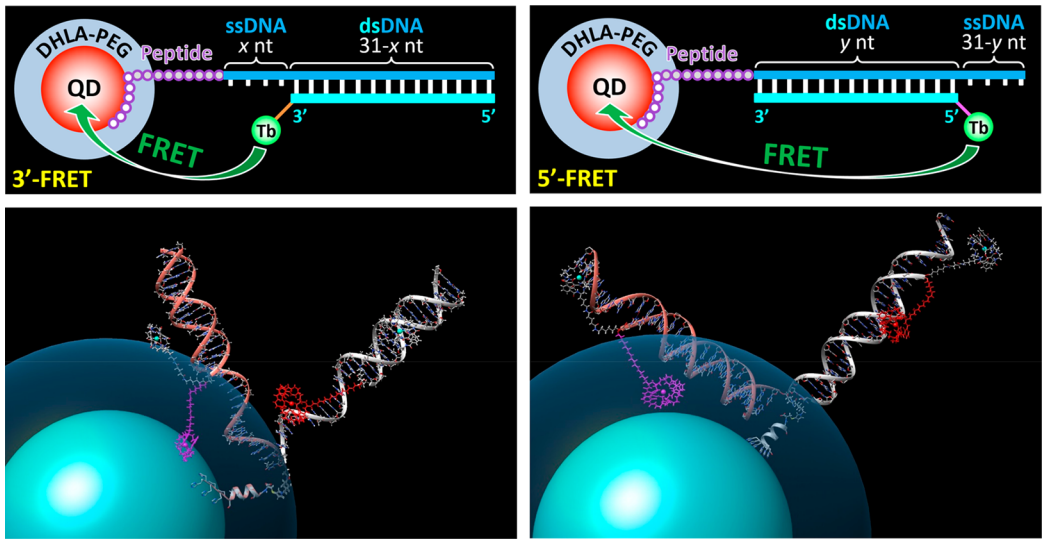

Figure 1. (Top) All QD-DNA systems consisted of the same 31 nt long ssDNA (blue), which was self-assembled *via* a His-tag-containing peptide (H_6SLGAAAGSGC + cross-linker) to the surface of QD625. Different ssDNA probes (cyan) conjugated with Tb on their 3′ or 5′ ends were used to investigate the conformation of the ssDNA-dsDNA (3′-FRET, x = 0, 2, 4, 6, 10, 14) and dsDNA-ssDNA (5′-FRET, y = 10, 14, 18, 22, 26) systems by Tb-to-QD FRET. Schematic presentation not to scale. (Bottom) Biomolecular modeling was used to calculate Tb-to-QD distance ranges in tangential (orange) and radial (gray) DNA-surface attachment configurations. Peptide and cross-linker placed most of the DNA outside the DHLA-PEG coating (dark blue) on the QD (cyan). DNA in the tangential configuration is partially in the DHLA-PEG ligand terminus to show the closest potential position. Flexible molecular linkers between Tb and DNA led to an additional distance variation as visualized by two extreme Tb positions for each DNA. Left image shows a 3′-FRET configuration with x = 14 nt. Right image shows a 5′-FRET configuration with y = 22 nt.

luminescence (PL) decays for temporal optical multiplexing,[25−33] which presents a powerful extension to the commonly used color multiplexing.[34,35] Although DNA distances can be extended nt per nt, there remain important limitations both for very short and very long FRET distances. Conjugating donor and acceptor to the respective 3′ and 5′ ends of complementary single-stranded DNA (ssDNA) strands usually leads to very close distances (0 nt) upon hybridization and a concomitant FRET efficiency close to 100%, which cannot be used for quantitatively analyzing donor−acceptor distances.[36,37] Longer distances are mainly affected by the FRET distance limit (close to 0% FRET efficiency), which is approximately 10 nm for efficient FRET pairs.[36,37] Molecular FRET rulers were shown to be functional between *ca.* 5 and 9 nm with dye−dye and QD−dye pairs (polyproline distance adjustment)[38] and between *ca.* 4 and 10 nm with Tb−dye pairs (double-stranded DNA (dsDNA) distance adjustment).[31] A detailed analysis of many distances and the resulting conformations over a long DNA strand conjugated to a QD under physiological conditions (in aqueous solution at low concentrations) would significantly improve the understanding of how DNA orients and behaves on nanoparticle surfaces, which, in turn, would provide important information for designing DNA-nanoparticle-based biosensors.

In the present study, we analyzed the conformation of a 31 nt long DNA, attached *via* a 5′ modified peptide-His_6 sequence (peptide-DNA) to a QD, when different Tb-conjugated complementary DNA probes hybridized at distances between 0 and 26 nt from the 5′ end of QD-conjugated DNA by time-resolved FRET and biomolecular modeling (Figure 1). Our results show that Tb-to-QD distances of up to 14 nm (center-to-center) can be precisely quantified using FRET theory with a dynamically averaged orientation and fitting the FRET-sensitized QD PL decay curves. In ssDNA conformation, the distance increase was linear with ∼0.15 nm/nt, the orientation of the DNA on the QD surface was more flexible, and the conformation more dense compared to dsDNA. In dsDNA conformation, the distance increase was also linear but with ∼0.31 nm/nt, and the orientation of the DNA was in almost perfect agreement with vertical attachment to the QD surface. All 11 conformations (0, 2, 4, 6, 10, and 14 nt for "3′-FRET" on ssDNA and 10, 14, 18, 22, and 26 nt for "5′-FRET" on dsDNA) showed distinct PL decay curves and DNA-concentration-dependent time-gated FRET ratios that demonstrated the feasibility of quantitative DNA biosensing at many different Tb-QD distances for temporal multiplexing. Our results show that, despite the relatively large nanoparticle dimensions, QD-DNA conjugates can be used as precise nanometric FRET rulers over long distances and that all of the applied distances between *ca.* 7 and 14 nm can be used for quantitative DNA analysis in a low nM concentration range.

RESULTS AND DISCUSSION

FRET DNA-Conjugates (Figure 1). The FRET pair consisted of a Lumi4-Tb donor (Tb)[39] and a DHLA-PEG-OMe (dihydrolipoic acid-appended poly(ethylene glycol))-coated Qdot625 acceptor (QD625).[40−43] Although QD625 has minor facets that make it not perfectly spherical, it is best approximated as a sphere with a diameter of 9.2 ± 0.8 nm.[40,44] The DHLA-PEG ligands (see Scheme S1 for chemical structure) extend 2.85 nm from the QD625 surfaces.[45] As shown in Figure 2, pulsed UV light (337.1 nm) efficiently excites both Tb and QD625, leading to four main Tb PL bands between 450 and 650 nm and one QD PL band around 625 nm. Due to their short PL lifetime (∼ns), the QDs decay quickly to their ground states and become available as FRET acceptors for the long PL lifetime (∼ms) Tb donors. This large difference of PL lifetimes leads to FRET-quenched Tb PL and FRET-sensitized QD PL with the same PL decay times (τ_{DA} =

DOI: 10.1021/acsnano.8b07137
ACS Nano 2019, 13, 505−514

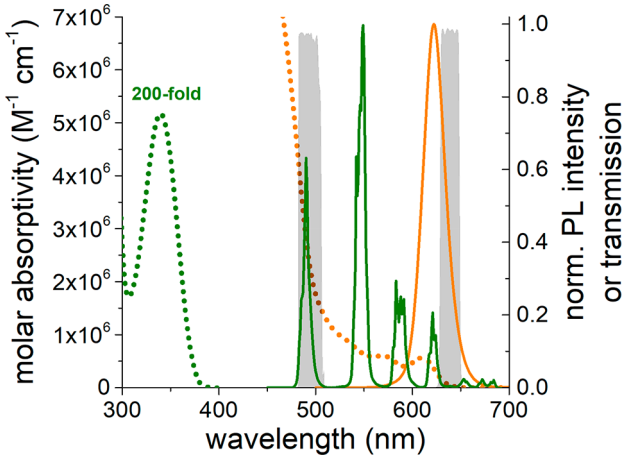

Figure 2. Absorption (dotted) and steady-state PL emission (solid) spectra of Tb (green; 450−700 nm; resolution: 0.5 nm; excitation: 365 ± 1 nm; concentration: 500 nM; solvent: 100 mM HEPES buffer pH 7.4) and QD625 (orange; 500−700 nm; resolution: 0.5 nm; excitation: 400.0 ± 2.5 nm; concentration: 10 nM; solvent: 100 mM Na-tetraborate + 0.1 M NaCl buffer pH 8.5) and filter transmission spectra (gray) used for Tb donor and QD acceptor time-resolved PL detection.

τ_{AD}).[19,46] The complete overlap of the Tb donor PL emission spectrum with the QD absorption spectrum and the very large molar absorptivity of QD625 (Figure 2) resulted in a spectral overlap integral of $J = 8.4 \times 10^{16}$ M^{-1} cm^{-1} nm^4 and a Förster distance (donor−acceptor distance for which FRET is 50% efficient) of $R_0 = 10.3$ nm (see eqs 1 and 2 and Materials and Methods section for details).[36,37] For minimal spectral crosstalk between the Tb and QD, PL decays were measured at 494 ± 12 nm for Tb and 639 ± 10 nm for QD625 (see Figure 2 for filter transmission spectra).

The main 31 nt long DNA strand (see Table 1 for sequences of all DNA used in our study) was attached *via* metal-affinity-mediated self-assembly (hexa-histidine: His_6) directly to the Zn-rich surface of QD625.[45,47] The His_6 was appended to 10 additional amino acids (SLGAAAGSGC) and a succinimidyl 4-(N-maleimidomethyl)cyclohexane-1-carbonate (SMCC) heterobifunctional cross-linker (see Scheme S2 for chemical structure) that extended the major part of the DNA beyond the DHLA-PEG coating on the QD625 surface (*cf.* Figure 1 bottom), such that the conformational freedom of the DNA was not restrained. The peptide-DNA strands assembled to the QD surface in a random manner as previously confirmed.[12,48]

We estimate that QD625 (diameter of 9.2 ± 0.8 nm, *vide supra*) can accommodate more than 100 peptides on its surface based on previous experimental work.[49] Given these assumptions, based on using a maximum ratio of 20 peptide-DNA per QD (10 nM peptide-DNA per 0.5 nM QD), we expect that the peptide-DNAs do not interact with each other. The Tb donor was brought into FRET proximity of the QD by hybridization of different Tb-DNA probes to the main QD-DNA strand. The distance between the first nt on the 5′ end of peptide-DNA and the Tb (on the 3′ or 5′end depending on the configuration) was adjusted in 11 different configurations between 0 and 26 nt, which resulted in Tb distances of 0 to 14 ssDNA bases and 10 to 26 dsDNA base pairs after the peptide extension from the QD (*cf.* Figure 1). We followed the strategy of separating the DNA strands of Tb donor and QD acceptor to investigate both ssDNA (3′-FRET) and dsDNA (5′-FRET) configurations on the same QD-DNA conjugate. Attachment of QD and Tb on the same peptide-DNA would have required different lengths of peptide-DNA. Another reason was the use of constant concentrations of Tb and QD for all experiments (without performing additional control experiments under different conditions), which was possible by adding the peptide-DNA to a predefined solution of Tb-DNA and QD625 (see Materials and Methods section). Because short dsDNA (<10 base pairs) were not stable under our experimental conditions, we could not use additional unlabeled strands to keep the full length of the DNA double-stranded.

Time-Resolved Tb-to-QD FRET DNA-Nanoruler and Distance Modeling. For all 11 configurations, PL decays of both the Tb donor and the QD625 acceptor were measured in a time range between 0 and 8 ms (Figures S1−S11). To distinguish between FRET and non-FRET contributions (from nonquenched Tb and directly excited QDs) and to be able to analyze various independent PL decay curves, the concentrations of Tb-DNA and QD625 were kept constant (20 nM Tb-DNA and 0.5 nM QD625), whereas the concentration of the peptide-DNA was varied (0, 2, 4, 6, 8, 10, and 20 nM). This strategy provided one background and six independent FRET measurements per configuration and a proof-of-concept system for a quantitative (signal over concentration) DNA hybridization assay. Figure 3 shows representative QD625 PL decay curves for all configurations at constant concentrations of 20 nM peptide-DNA (PL decays for both Tb and QD625 at different peptide-DNA concentrations are shown in Figures S1−S11). As expected from FRET theory, the increasing Tb-to-QD distances led to increasing FRET-sensitized lifetimes of

Table 1. DNA Oligonucleotides Used in the Study

	sequence 5′-3′	modification	Tb/DNA ratio
Tb-DNA (for 0 base)	CTACCTGCACTATGAGCACTTTGTCGAGCTA	3′-C_6 amino	0.79
Tb-DNA (for 2 base ssDNA)	CTACCTGCACTATGAGCACTTTGTCGAGC	3′-C_6 amino	0.88
Tb-DNA (for 4 base ssDNA)	CTACCTGCACTATGAGCACTTTGTCGA	3′-C_6 amino	0.75
Tb-DNA (for 6 base ssDNA)	CTACCTGCACTATGAGCACTTTGTC	3′-C_6 amino	0.77
Tb-DNA (for 10 base ssDNA)	CTACCTGCACTATGAGCACTT	3′-C_6 amino	0.97
Tb-DNA (for 14 base ssDNA)	CTACCTGCACTATGAGC	3′-C_6 amino	0.82
Tb-DNA (for 10 bps dsDNA)	TGTCGAGCTA	5′-C_3 amino	0.85
Tb-DNA (for 14 bps dsDNA)	ACTTTGTCGAGCTA	5′-C_3 amino	0.81
Tb-DNA (for 18 bps dsDNA)	GAGCACTTTGTCGAGCTA	5′- C_3 amino	0.71
Tb-DNA (for 22 bps dsDNA)	CTATGAGCACTTTGTCGAGCTA	5′-C_3 amino	0.84
Tb-DNA (for 26 bps dsDNA)	TGCACTATGAGCACTTTGTCGAGCTA	5′-C_3 amino	0.90
Peptide-DNA	TAGCTCGACAAAGTGCTCATAGTGCAGGTAG	5′-H6SLGAAAGSGC-SMCC-amino	–

DOI: 10.1021/acsnano.8b07137
ACS Nano 2019, 13, 505−514

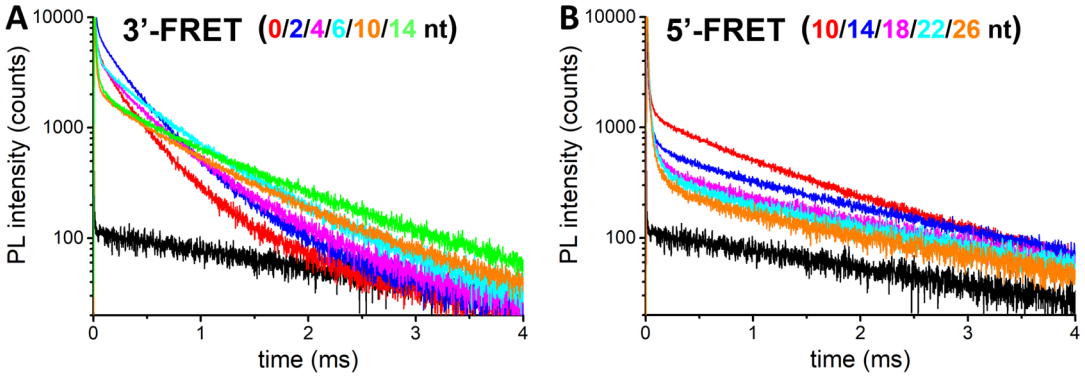

Figure 3. Time-resolved PL decay curves of QD625 in the different FRET configurations (A, ssDNA or 3′-FRET; B, dsDNA or 5′-FRET) shown in Figure 1. Concentrations of peptide-DNA were 20 nM for all curves. All samples were measured in 20 mM Tris-Cl, 500 mM NaCl, 0.1% BSA, pH 8.0, excited at 337.1 nm (nitrogen laser), and detected at 639 ± 10 nm. PL decay curves of different concentrations for both Tb and QD625 are shown in Figures S1−S11. Black curves present spectral crosstalk of Tb (only Tb-DNA without peptide-DNA and QD625) inside the QD625 detection channel.

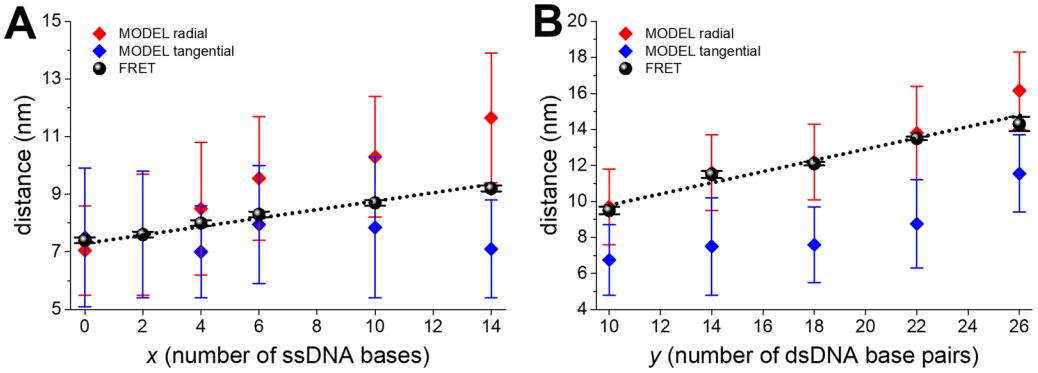

Figure 4. Tb-donor-to-QD-acceptor distances measured by FRET-sensitized PL of QD625 (black dots) and modeled in radial (red diamonds) and tangential (blue diamonds) configuration (see Figure 1) for 3′-FRET (A) and 5′-FRET (B). Error bars for models present the closest and furthest distance of Tb from the QD in the two different configurations. Error bars for FRET present maximum PL lifetime errors from three measurements with different concentrations. See Figures S1−S12 and Tables S1 and S2 for details.

the PL decays, all of which can be readily distinguished without lifetime fitting of the PL decay curves. Such fine-tuning of PL decays *via* displacement of the Tb donor by only a few nt demonstrates the high distance sensitivity of FRET and the possibility to extend nanoparticle-based temporal multiplexing beyond two distinct PL decays.[31]

In order to understand the orientation of the ssDNA and dsDNA on the nanoparticle surface and the distance tunability or sensitivity (distance per nt) in these two open and hybridized configurations, we fitted PL decay curves for three peptide-DNA concentrations (6, 8, and 10 nM) for both FRET-sensitized QD625 PL and FRET-quenched Tb PL (see Materials and Methods section for fitting procedure and Supporting Information for detailed fitting results). All PL decay curves showed multiexponential decays (eqs 3 and 4),[37] which consist of a monoexponential contribution from unquenched Tb (τ_D = 2.75 ± 0.05 ms, from Tb that do not participate in FRET) and a multiexponential contribution from FRET, owing to a Tb-to-QD distance distribution caused by the flexibility of the DNA and the linker between Tb and DNA (cf. Figure 1 bottom) and the shape of QD625, which is not perfectly spherical and monodisperse (*vide supra*). Although the single FRET-sensitized PL lifetimes (τ_{AD}) of QD625 and FRET-quenched PL lifetime (τ_{DA}) of Tb are the same, the average FRET-sensitized acceptor lifetime must be corrected by the FRET rates of each single component (eqs 8 and 9).[37]

The average FRET lifetimes ($\langle\tau_{AD}\rangle$ and $\langle\tau_{DA}\rangle$) can then be used to calculate the average Tb-to-QD distances (eqs 6 and 10) and FRET efficiencies (eqs 7 and 11).[37] Due to the much weaker PL background of unquenched Tb in the QD acceptor detection channel (*cf.* Figures S1−S11), this channel usually provides better fitting results.[31,50] Tb-to-QD distances were also calculated by biomolecular modeling. Closest and furthest distances for both parallel and vertical orientations of the peptide-DNA on the QD625 surface were calculated (Table S2). The average theoretical distances and the FRET distances (calculated from QD625 acceptor PL decays) of all configurations are shown in Figure 4. Tb donor PL results, which are very similar to the QD acceptor results for shorter distances but deviate for longer distances, are shown in Figure S12.

For both configurations (single and double-stranded), the FRET results show a linearly increasing Tb-to-QD distance with the number of bases. With 0.31 nm per base pair, the dsDNA distance increase is approximately twice as large as the one of ssDNA (0.15 nm per base). While the dsDNA distance is in very good agreement with the literature (~0.33 nm length per base pair)[24] and confirms the excellent long-range precision of our FRET nanoruler, the one for ssDNA is relatively short compared to previous studies. In a single-molecule FRET approach, Murphy *et al.* investigated a similar ssDNA-dsDNA system, which contained a Cy3 donor on the

DOI: 10.1021/acsnano.8b07137
ACS Nano 2019, 13, 505−514

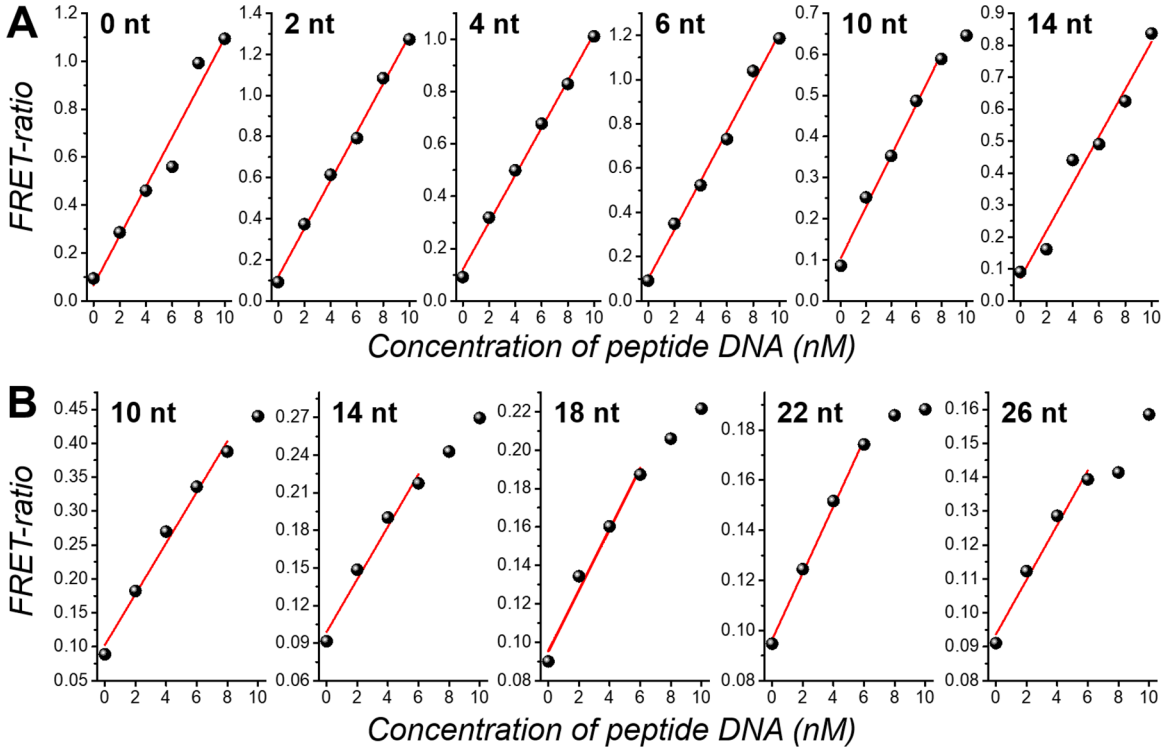

Figure 5. Calibration curves of prototypical DNA hybridization assays showing increasing time-gated FRET ratios (QD625 PL intensity divided by Tb PL intensity in a time gate from 0.1 to 2.0 ms after the excitation pulse) with increasing peptide-DNA concentrations for all 3′-FRET (A) and 5′-FRET (B) configurations.

3′ end of ssDNA and a Cy5 acceptor on the 5′ end of a 18 nt long ssDNA probe that was hybridized to the ssDNA and attached *via* a 3′-biotin functionalization to a streptavidin-coated microscope slide.[51] At similar buffer conditions (12−20 mM Tris, pH 8.0, 400 mM NaCl) they found ssDNA lengths of 4.4, 5.0, 5.3, 5.6, 6.0, and 7.1 nm for 10, 15, 17, 23, 27, and 40 nt lengths of poly dT ssDNA, respectively. These values correspond to 0.44, 0.33, 0.31, 0.24, 022, and 0.18 nm per base, and taking into account that our ssDNA lengths varied between 0 and 14 nt, a distance above 0.33 nm per base would have been expected from the single-molecule FRET study. On the other hand, our ssDNA had a variable sequence, whereas the single-molecule study investigated poly dT ssDNA. Moreover, the conditions of a DNA attached to a nanoparticle (on the ssDNA end) in solution could be quite different from a DNA attached to a microscopy slide (on the dsDNA end). Taking into account the almost perfect linearity determined by five different lengths over 14 nt and the relatively good agreement with the model data (Figure 4A), it can be assumed that the value of 0.15 nm per base is realistic for our QD-DNA system. This unexpectedly short distance also shows the necessity of measuring the actual DNA conformation on a nanoparticle surface instead of assuming a value from a study with similar but still significantly different conditions.

Another very interesting finding from the FRET data concerns the orientation and conformation of the DNA on the QD surface. The experimental distances present average orientations and/or conformations over all peptide-DNAs per QD and over the ensemble of QDs. This averaging also includes possible modifications of orientations and conformations during the FRET process. Taking into account the spatially distributed attachment of several peptide-DNAs on the QD surface at a relatively low DNA/QD ratio that avoids interactions between the different DNA strands, the average distance values reflect the actual overall orientation/conformation of the QD-DNA conjugates in solution. Moreover, the linear distance increase over several lengths of both ssDNA (3′-FRET configuration) and dsDNA (5′-FRET configuration) is another important piece of evidence that the average FRET distances provide meaningful information concerning orientation and conformation. The ssDNA extensions measured by FRET (Figure 4A) can be adequately approximated by an average of tangential and radial orientations, whereas the dsDNA extension measured by FRET (Figure 4B) overlaps quite well with radial orientation (*cf.* Figure 1 for theoretical tangential and radial DNA orientations). From the structural point of view, these results reflect a flexible ssDNA that can take any orientation on the QD surface and a very stiff dsDNA that does not bend on the QD surface. They also show that the cross-linker between peptide and DNA does not provide rotational freedom, which would have led to the same flexibility for both ssDNA and dsDNA. This lack of free rotation can be explained by the position of the linker within the DHLA-PEG ligand terminus. From the conformational point of view, the results reflect a denser conformation of ssDNA (~0.15 nm per base, Figure 4A) compared to dsDNA (~0.31 nm per base pair, Figure 4B). Taking into account the larger structural and conformational freedom of ssDNA, we assume both effects (flexibility and density) are responsible for the actual distance. Although this different behavior between ssDNA and dsDNA is not surprising, it cannot be simply taken for granted for DNA attached to the surface of a nanoparticle. The experimental determination by FRET at low concentrations and physiological conditions provides highly important information concerning the natural structure of DNA-nanoparticle conjugates. Because many DNA-based nanosensors

DOI: 10.1021/acsnano.8b07137
ACS Nano 2019, 13, 505−514

depend on distances and conformations that change from single ssDNA (probe alone) to dsDNA (probe-target hybridization) and that are influenced by the environment, the attachment chemistry, and other experimental conditions, knowledge about the conformational behavior within such a sensor will be extremely valuable to design and optimize the biological recognition and signal generation.

Prototypical DNA Hybridization Assays. In addition to the structural and conformational information, the precise distance tuning also allows for the generation of many distinct PL decay curves of FRET-sensitized QD625 PL (*cf.* Figure 3). Such PL decays can be used for higher order multiplexed quantification of biomarkers or optical barcoding of cells.[31,32,35] Distinct temporal detection windows (time-gated PL intensity detection) after pulsed excitation were already used to distinguish different DNAs or RNAs by Tb-QD and Tb-dye FRET[31,35] or different cells by Tb/Eu-QD FRET.[32] To demonstrate target quantification by concentration-dependent FRET ratios (ratio of time-gated intensities of QD625 and Tb PL), we used peptide-DNA concentrations between 0 and 10 nM while keeping all other assay components constant. As shown in Figure 5, all 11 configurations provided a FRET-ratio increase (linear up to at least 6 nM) over peptide-DNA concentration. Despite the relatively low assay sensitivities (slopes of the calibration curves) and the deviations from the linear FRET-ratio increase for the very long distance configurations (14, 18, 22, and 26 nt in 5′-FRET configurations with donor–acceptor distances of more than 11 nm, *cf.* Figure 4B), all FRET constructs could be used for quantifying DNA at low nanomolar concentrations. Although such systems need to be adapted to real targets (in our case both QD-peptide-DNA and Tb-DNA were DNA probes), the proof-of-concept hybridization assays demonstrated the possible application of DNA-based Tb-to-QD distance tuning for higher order temporal multiplexing that can also be combined with several different QD colors.[52]

CONCLUSION

In summary, we have extensively investigated the orientation of a 31 nt long DNA attached *via* a His_6-peptide linker to a QD by Tb-to-QD FRET and biomolecular modeling. Our results show that time-resolved analysis of FRET-sensitized QD PL can be used to precisely measure the distances along the QD-DNA conjugate by hybridization of different Tb-DNA probes at different positions of the QD-DNA. Long-range QD-to-Tb distances between *ca.* 7 and 14 nm (from center to center) significantly extended beyond previous FRET systems. The detailed investigation of 11 different DNA configurations on the nanoparticle surface and the comparison of the FRET results with biomolecular modeling allowed us to extract important conformational information from the FRET data. In single-stranded conformation, the DNA extended from the QD with ∼0.15 nm per base, and the denser and more flexible ssDNA could possibly take different orientations on the QD surface. In double-stranded conformation, the DNA extended with ∼0.31 nm per base pair, and the orientation was purely vertical, reflecting the stiffness of dsDNA. Determination of different lengths and orientations of ssDNA and dsDNA on nanoparticle surfaces under physiological conditions and at low nanomolar concentrations is highly important for an efficient development and optimization of hybridization-based DNA nanosensors, and our Tb-to-QD FRET ruler provided very useful information that should in principle be transferable to any other DNA-nanoparticle conjugate. Future applications of the Tb-to-QD FRET ruler can extend our initial studies to investigate different surface chemistries, DNA loading ratios, hybridization states, peptide linkers, and other modifications to better understand how the combinations of all these materials and functions determine the DNA orientation and/or conformation on QDs. In addition to the precise structural and conformational FRET analysis, we showed that the DNA distance tuning can be used to generate many distinct PL decay curves (with different average PL lifetimes), whose intensities were dependent on the peptide-DNA concentration, even for configurations with very long donor–acceptor distances (∼14 nm). Prototypical DNA-hybridization assays for all 11 configurations suggest that these Tb-to-QD FRET DNA constructs have a strong potential to significantly extend the multiplexing range of the recently developed time-gated temporal optical multiplexing concept.[31,32,35] Our results demonstrate that QDs, despite their relatively large sizes, can be used for precise structural and conformational analysis and extended temporal multiplexed detection of nucleic acid biomarkers and that the Tb-QD donor–acceptor FRET pair presents a useful optical tool for both diagnostic and biophysical applications.

MATERIALS AND METHODS

Materials. Lumi4-Tb-NHS was provided by Lumiphore Inc. (Berkeley, CA). 625 nm emitting proprietary QDs were provided by Invitrogen by Life Technologies (Carlsbad, CA) and functionalized with dihydrolipoic acid(DHLA)-appended poly(ethylene glycol) (PEG, MW ∼ 750) ligands (Scheme S1) in house.[38,45,50] Peptide-oligonucleotide was synthesized by Biosynthesis (Lewisville, Texas, USA). All other modified oligonucleotides were purified with HPLC from Eurogentec (Liège, Belgium). All sequences and modifications of nucleic acids used in this study are summarized in Table 1. Tris(hydroxymethyl)-aminomethane, bovine serum albumin, and HEPES were purchased from Sigma-Aldrich (St. Louis, MO, USA). NaCl was purchased from Duchefa (Netherlands). All chemicals were used as received. Water was purified by MAXIMA (USF Elga, UK). Zeba Spin Desalting Columns (7 kDa MWCO) were purchased from Thermo Fisher Scientific (Nîmes, France).

Tb-DNA conjugates were obtained by mixing Lumi4-Tb-NHS (8 mM, lyophilized product dissolved in anhydrous DMF) in concentration excess to amino-functionalized oligonucleotides in 100 mM carbonate buffer at pH 9.0. The mixtures were incubated overnight at 4 °C. The Tb-DNA conjugates were purified 3 times by Zeba Spin Desalting Columns (7 kDa MWCO). Tb concentrations were determined by absorbance measurements at 340 nm using a molar absorptivity of 26,000 M^{-1} cm^{-1} as provided by the manufacturer. DNA was quantified by absorbance measurements at 260 nm. Labeling ratios were determined by linear combination of the respective absorbance values of Tb and oligo within the Tb-DNA conjugates.

Spectroscopic Characterization. Absorption spectra (Lambda 35 UV/vis System, PerkinElmer) and emission spectra (for Tb: FluoTime 300, PicoQuant; for QD625: Xenius, SAFAS) were recorded in 100 mM HEPES buffer (pH 7.4) for Tb and in 100 mM Na-tetraborate + 0.1 M NaCl buffer (pH 8.5) for QD625.

Tb-QD FRET Assays. All FRET assays were prepared in DNA hybridization buffer and contained 50 μL of Tb-DNA and 50 μL of 625 nm DHLA-PEG-OMe-capped QDs at constant concentrations to which 50 μL of peptide-oligonucleotides at different concentrations were added. The single sensor assays contained 20 nM of Tb-DNA, 0.5 nM of DHLA-PEG-OMe-capped QD, and increasing concentrations of peptide-DNA (from 0 nM to 10 nM), and all samples were prepared once. After sample preparation, they were incubated in black 96-well microtiter plates for 30 min at room temperature (22 °C) with an optimal working volume of 150 μL. PL decay curves were

DOI: 10.1021/acsnano.8b07137
ACS Nano 2019, 13, 505–514

acquired on a fluorescence plate reader (Edinburgh Instruments) using 4000 detection bins of 2 μs integration time and nitrogen laser (MNL 100, LTB Lasertechnik Berlin) excitation (337.1 nm, 20 Hz). Optical transmission bandpass filters were 494/20 (Semrock) for the Tb detection channel and 640/14 (Semrock) for the QD625 detection channel. FRET ratio values were used as a detection signal for the DNA hybridization assays. The FRET ratio was calculated by dividing the PL intensities of QD625 and Tb in a time-gated window between 0.1 and 2 ms after pulsed excitation. Calibration curves show increasing time-gated PL FRET ratio as a function of peptide-DNA concentration.

Photophysical Properties of Tb and QD and R_0 Calculation. A Förster distance (the donor−acceptor distance for which FRET is 50% efficient) of R_0 = 10.3 nm was calculated using the following equation:

$$R_0 = 0.02108(\kappa^2 \Phi_D n^{-4} J)^{1/6}\,\text{nm} \tag{1}$$

The orientation factor κ^2 was taken as 2/3 because of random orientation of donor and acceptor during the FRET time (dynamic averaging), which is well justified by the long PL lifetime of the Tb donors and the unpolarized emission (fast isotropic rotation). The refractive index was n = 1.35 (aqueous solution). The Tb-centered quantum yield was Φ_D = 0.81 ± 0.05. The overlap integral J was calculated by the following equation:

$$J = \int_{450\text{nm}}^{650\text{nm}} I_D(\lambda)\varepsilon_A(\lambda)\lambda^4 d\lambda \tag{2}$$

where $I_D(\lambda)$ is the emission intensity from the area-normalized (to unity) emission spectrum of Tb donor and $\varepsilon_A(\lambda)$ is the molar absorptivity of the acceptor. The spectra are shown in Figure 2.

Time-Resolved PL Decay Curves and Fit Results of Tb and QD for Tb-QD-DNA Configurations with 0, 2, 4, 6, 10, and 14 Base ssDNAs and 10, 14, 18, 22, 26 Base dsDNAs Separation. All PL decay curves were fit using multiexponential intensity decay functions with a starting time point for the fit of t_0, which corresponds to a short delay between the start of the actual PL decay and the start of the fit (due to very strong background fluorescence in the short time range, the fits usually start after a few tens of μs as indicated above each fit result table). The PL intensity decay is defined by the following equation:

$$I = \sum_i A_{i-\text{fit}} \exp\left(-\frac{t - t_0}{\tau_i}\right) = \sum_i A_i \exp\left(-\frac{t}{\tau_i}\right) \tag{3}$$

"Fast" software from Edinburgh Instruments was used for fitting all PL decay curves. As the actual decay starts before t_0, the amplitudes ($A_{i-\text{fit}}$), which are used to calculate average PL lifetimes, need to be corrected using the following equation:

$$A_{i-\text{fit}} \exp\left(-\frac{t - t_0}{\tau_i}\right) = A_i \exp\left(-\frac{t}{\tau_i}\right) \Rightarrow A_i = A_{i-\text{fit}} \exp\left(-\frac{t_0}{t}\right) \tag{4}$$

Because all PL decay curves (in particular those from the Tb donor detection channel) contain a certain amount of unquenched Tb decay, this "pure Tb" decay time (τ_D) was used as a fixed decay time in the multiexponential fit functions. τ_D was determined for each set of experiments (in the Tb-donor channel and the QD-acceptor channel) by fitting the PL decay curves for a sample in which only Tb-DNA was present. τ_D (in ms) was also used to determine the Tb-centered PL quantum yield ($\Phi_{Tb} = \tau_D$ /3.45 ms; 3.45 ms is the Tb lifetime for Φ_{Tb} = 1), which is the quantum yield that needs to be used for calculating the Förster distance individually for each DNA system. Tb donor decays were fit by a three-exponential function (with τ_i corresponding to τ_D, τ_{DA1}, and τ_{DA2}) from Figures S1−S7 and by a two-exponential function (with τ_i corresponding to τ_D and τ_{DA1}) from Figures S8−S11, whereas QD acceptor decays were fit with a four-exponential function (with τ_i corresponding to τ_D, τ_{AD1}, τ_{AD2}, and τ_{AD3}).

For Tb donor decays, the amplitude averaged decay time τ_{DA} was used as FRET decay time to calculate the Tb-QD distance r:

$$\langle\tau_{DA}\rangle = \frac{\sum A_i\tau_i}{\sum A_i} \tag{5}$$

with τ_i corresponding to the FRET-quenched PL decay times τ_{DA1} and τ_{DA2} (the pure Tb decay with τ_D is not taken into account).

$$r = R_0\left(\frac{\langle\tau_{DA}\rangle}{\tau_D - \langle\tau_{DA}\rangle}\right)^{1/6} \tag{6}$$

The FRET efficiency was calculated by

$$E_{FRET} = \frac{{R_0}^6}{{R_0}^6 + r^6} = 1 - \frac{\langle\tau_{DA}\rangle}{\tau_D} \tag{7}$$

For the QD acceptor, the amplitude averaged decay time $\langle\tau_{AD}\rangle$ was used as FRET decay time to calculate the Tb-QD distance r. The amplitudes A_i must be corrected by the FRET rates (k_{FRET-i}) to take into account the FRET-efficiency dependent excitation of the acceptors:

$$k_{FRET-i} = \frac{1}{\tau_{ADi}} - \frac{1}{\tau_D} \tag{8}$$

and

$$\langle\tau_{AD}\rangle = \sum\left(\frac{(A_i/k_{FRET-i})}{\sum(A_i/k_{FRET-i})}\tau_i\right) \tag{9}$$

with τ_i corresponding to the FRET-sensitized PL decay times τ_{AD2} and τ_{AD3} (the pure Tb decay with τ_D and the very short QD-background decay with τ_{AD1} are not taken into account).

The Tb-QD distance r was then calculated by

$$r = R_0\left(\frac{\langle\tau_{AD}\rangle}{\tau_D - \langle\tau_{AD}\rangle}\right)^{1/6} \tag{10}$$

The FRET efficiency was calculated by

$$E_{FRET} = \frac{{R_0}^6}{{R_0}^6 + r^6} = 1 - \frac{\langle\tau_{AD}\rangle}{\tau_D} \tag{11}$$

Due to the relatively low FRET efficiencies for the configurations with long Tb-QD donor−acceptor distances (18, 22, and 26 dsDNAs separation), the QD acceptor decay fits from Figures S9−S11 required further adjustment of the fit parameters. Here, the amplitude of pure Tb decay (from spectral crosstalk in the acceptor channel) was fixed to the following value:[31]

$$A_D = \frac{A_{A0}A_{DA0}}{A_{D0}} \tag{12}$$

where $A_{A0}$is the amplitude of the pure Tb decay curve in the QD detection channel and A_{DA0} and A_{D0} are the amplitudes of the Tb PL decay curves in the Tb detection channel, in the presence and in the absence of peptide-DNA, respectively.

Figures S1−S11 show the PL decay curves (and fitted PL decay curves) in the Tb donor and QD acceptor channels for all DNA systems (0, 2, 4, 6, 10, and 14 ssDNAs, and 10, 14, 18, 22, 26 dsDNAs). The corresponding fit results (all decay times given in μs) are given directly below the figures.

Biomolecular Modeling. The double-stranded DNA (dsDNA) model was constructed using make-na,[53] a web-based utility that builds a 3D model from a linear DNA sequence using Nucleic Acid Builder.[54,55] The model was built using the sequence CTACCTG-CACTATGAGCACTTTGTCGAGCTA. All DNA models were derived from this initial model by removing part of the A or B chain to produce a double-stranded model with a single-stranded segment at one end. Single-stranded DNA (ssDNA) can be thought of as an idealized flexible polymeric molecule without base pairing and

DOI: 10.1021/acsnano.8b07137
ACS Nano 2019, 13, 505−514

stacking. The freely jointed chain model and worm-like chain model have been used by other investigators to characterize long ssDNA.[56,57] Under physiological conditions, ssDNA is usually composed of stacked domains interspaced with random-coil domains. In the cases considered in this study, the ssDNA has been assumed to have a random-coil conformation. Thus distance estimates for models with ssDNA close to the QD surface all start with Tb at or close to the QD surface. Note: Considerable uncertainty exists in all models in which the ssDNS was close to the QD surface due to the limitations of the modeling software used when applied to ssDNA. The thickness of the DHLA-PEG capping ligand on the QD surface was previously estimated to be 2.85 nm and is represented in the figures as a shell 2.85 nm larger than the QD. The structure of Lumi4-Tb (Tb) is based on published coordinates for this complex.[39] All other models were created using tools in UCSF Chimera (version 1.4.1).[58] Energy minimization was carried out in Chimera using built in features including ANTECHAMBER (version 1.27) and the AM1-BCC method of calculating charges.[59] To explore the range of possible distances between the Tb and QD, surface torsion angles in the linker used to attach the terbium to the DNA were adjusted to determine minimum and maximum separations.

ASSOCIATED CONTENT

Supporting Information

The Supporting Information is available free of charge on the ACS Publications website at DOI: 10.1021/acsnano.8b07137.

Chemical structures of the DHLA-PEG ligand (Scheme S1) and the SMCC cross-linker (Scheme S2); PL decay curves of QD acceptor and Tb donor at different peptide-DNA concentrations and PL lifetime fit results for all 3′-FRET and 5′-FRET configurations (Figures S1−S11); Modeling *vs* FRET-quenched Tb-donor PL lifetimes for distance determination (Figure S12); All distances and FRET-efficiencies determined by FRET PL lifetime fitting (Table S1); All distances determined by biomolecular modeling (Table S2) (PDF)

AUTHOR INFORMATION

Corresponding Author

*E-mail: niko.hildebrandt@u-psud.fr.

ORCID

Kimihiro Susumu: 0000-0003-4389-2574
Igor L. Medintz: 0000-0002-8902-4687
Niko Hildebrandt: 0000-0001-8767-9623

Author Contributions

⊥These authors contributed equally.

Notes

The authors declare no competing financial interest.

ACKNOWLEDGMENTS

We thank Lumiphore, Inc. for the gift of Lumi4 reagents. This work was partially funded by the European Commission (H2020-FET-Open project PROSEQO) and the French National Research Agency (ANR projects “Neutrinos”, “AMPLIFY”, and “PhenX”). J.G. acknowledges the China Scholarship Council (CSC) for her Ph.D. fellowship. I.M. acknowledges ONR, NRL, the NRL-Nanosciences Institute and a LUCI grant in support of the VBFF program through the OSD. N.H. acknowledges the Institut Universitaire de France (IUF) for financial support.

REFERENCES

(1) Abu-Salah, K. M.; Zourob, M. M.; Mouffouk, F.; Alrokayan, S. A.; Alaamery, M. A.; Ansari, A. A. DNA-Based Nanobiosensors as an Emerging Platform for Detection of Disease. *Sensors* **2015**, *15*, 14539−14568.

(2) Dehghani, S.; Nosrati, R.; Yousefi, M.; Nezami, A.; Soltani, F.; Taghdisi, S. M.; Abnous, K.; Alibolandi, M.; Ramezani, M. Aptamer-Based Biosensors and Nanosensors for the Detection of Vascular Endothelial Growth Factor (VEGF): A Review. *Biosens. Bioelectron.* **2018**, *110*, 23−37.

(3) Kundu, A.; Nandi, S.; Nandi, A. K. Nucleic Acid Based Polymer and Nanoparticle Conjugates: Synthesis, Properties and Applications. *Prog. Mater. Sci.* **2017**, *88*, 136−185.

(4) Oh, J. H.; Park, D. H.; Joo, J. H.; Lee, J. S. Recent Advances in Chemical Functionalization of Nanoparticles with Biomolecules for Analytical Applications. *Anal. Bioanal. Chem.* **2015**, *407*, 8627−8645.

(5) Rasheed, P. A.; Sandhyarani, N. Electrochemical DNA Sensors Based on the Use of Gold Nanoparticles: A Review on recent developments. *Microchim. Acta* **2017**, *184*, 981−1000.

(6) Samanta, A.; Medintz, I. L. Nanoparticles and DNA - A Powerful and Growing Functional Combination in Bionanotechnology. *Nanoscale* **2016**, *8*, 9037−9095.

(7) Shi, J. Y.; Tian, F.; Lyu, J.; Yang, M. Nanoparticle Based Fluorescence Resonance Energy Transfer (FRET) for Biosensing Applications. *J. Mater. Chem. B* **2015**, *3*, 6989−7005.

(8) Zhao, W. W.; Xu, J. J.; Chen, H. Y. Photoelectrochemical DNA Biosensors. *Chem. Rev.* **2014**, *114*, 7421−7441.

(9) Sapsford, K. E.; Algar, W. R.; Berti, L.; Gemmill, K. B.; Casey, B. J.; Oh, E.; Stewart, M. H.; Medintz, I. L. Functionalizing Nanoparticles with Biological Molecules: Developing Chemistries that Facilitate Nanotechnology. *Chem. Rev.* **2013**, *113*, 1904−2074.

(10) Banerjee, A.; Pons, T.; Lequeux, N.; Dubertret, B. Quantum Dots-DNA Bioconjugates: Synthesis to Applications. *Interface Focus* **2016**, *6*, 20160064.

(11) Zhang, C. L.; Ding, C. P.; Xiang, D. S.; Li, L.; Ji, X. H.; He, Z. K.; Xian, Y. Z. DNA Functionalized Fluorescent Quantum Dots for Bioanalytical Applications. *Chin. J. Chem.* **2016**, *34*, 317−325.

(12) Blanco-Canosa, J. B.; Wu, M.; Susumu, K.; Petryayeva, E.; Jennings, T. L.; Dawson, P. E.; Algar, W. R.; Medintz, I. L. Recent Progress in the Bioconjugation of Quantum Dots. *Coord. Chem. Rev.* **2014**, *263*, 101−137.

(13) Samanta, A.; Deng, Z. T.; Liu, Y. Infrared Emitting Quantum Dots: DNA Conjugation and DNA Origami Directed Self-Assembly. *Nanoscale* **2014**, *6*, 4486−4490.

(14) Hu, J.; Wang, Z. Y.; Li, C. C.; Zhang, C. Y. Advances in Single Quantum Dot-Based Nanosensors. *Chem. Commun.* **2017**, *53*, 13284−13295.

(15) Wen, L.; Qiu, L. P.; Wu, Y. X.; Hu, X. X.; Zhang, X. B. Aptamer-Modified Semiconductor Quantum Dots for Biosensing Applications. *Sensors* **2017**, *17*, 1736.

(16) Wang, G. L.; Li, Z.; Ma, N. Next-Generation DNA-Functionalized Quantum Dots as Biological Sensors. *ACS Chem. Biol.* **2018**, *13*, 1705−1713.

(17) Freeman, R.; Girsh, J.; Willner, I. Nucleic Acid/Quantum Dots (QDs) Hybrid Systems for Optical and Photoelectrochemical Sensing. *ACS Appl. Mater. Interfaces* **2013**, *5*, 2815−2834.

(18) Algar, W. R.; Kim, H.; Medintz, I. L.; Hildebrandt, N. Emerging Non-Traditional Förster Resonance Energy Transfer Configurations with Semiconductor Quantum Dots: Investigations and Applications. *Coord. Chem. Rev.* **2014**, *263*, 65−85.

(19) Hildebrandt, N.; Spillmann, C. M.; Algar, W. R.; Pons, T.; Stewart, M. H.; Oh, E.; Susumu, K.; Diaz, S. A.; Delehanty, J. B.; Medintz, I. L. Energy Transfer with Semiconductor Quantum Dot Bioconjugates: A Versatile Platform for Biosensing, Energy Harvesting, and Other Developing Applications. *Chem. Rev.* **2017**, *117*, 536−711.

(20) Stanisavljevic, M.; Krizkova, S.; Vaculovicova, M.; Kizek, R.; Adam, V. Quantum Dots-Fluorescence Resonance Energy Transfer-

DOI: 10.1021/acsnano.8b07137
ACS Nano 2019, 13, 505−514

Based Nanosensors and Their Application. *Biosens. Bioelectron.* **2015**, *74*, 562−574.
(21) Noor, M. O.; Petryayeva, E.; Tavares, A. J.; Uddayasankar, U.; Algar, W. R.; Krull, U. J. Building from the "Ground" Up: Developing Interfacial Chemistry for Solid-Phase Nucleic Acid Hybridization Assays Based on Quantum Dots and Fluorescence Resonance Energy Transfer. *Coord. Chem. Rev.* **2014**, *263*, 25−52.
(22) Geissler, D.; Hildebrandt, N. Recent Developments in Förster Resonance Energy Transfer (FRET) Diagnostics Using Quantum Dots. *Anal. Bioanal. Chem.* **2016**, *408*, 4475−4483.
(23) Cardoso Dos Santos, M.; Hildebrandt, N. Recent Developments in Lanthanide-to-Quantum Dot FRET Using Time-Gated Fluorescence Detection and Photon Upconversion. *TrAC, Trends Anal. Chem.* **2016**, *84*, 60−71.
(24) Mandelkern, M.; Elias, J. G.; Eden, D.; Crothers, D. M. The Dimensions of DNA in Solution. *J. Mol. Biol.* **1981**, *152*, 153−161.
(25) Cui, H. H.; Valdez, J. G.; Steinkamp, J. A.; Crissman, H. A. Fluorescence Lifetime-Based Discrimination and Quantification of Cellular DNA and RNA with Phase-Sensitive Flow Cytometry. *Cytometry* **2003**, *52A*, 46−55.
(26) Grabolle, M.; Kapusta, P.; Nann, T.; Shu, X.; Ziegler, J.; Resch-Genger, U. Fluorescence Lifetime Multiplexing with Nanocrystals and Organic Labels. *Anal. Chem.* **2009**, *81*, 7807−7813.
(27) Hoffmann, K.; Behnke, T.; Drescher, D.; Kneipp, J.; Resch-Genger, U. Near-Infrared-Emitting Nanoparticles for Lifetime-Based Multiplexed Analysis and Imaging of Living Cells. *ACS Nano* **2013**, *7*, 6674−6684.
(28) Hoffmann, K.; Behnke, T.; Grabolle, M.; Resch-Genger, U. Nanoparticle-Encapsulated Vis- and NIR-Emissive Fluorophores with Different Fluorescence Decay Kinetics for Lifetime Multiplexing. *Anal. Bioanal. Chem.* **2014**, *406*, 3315−3322.
(29) Lu, Y. Q.; Lu, J.; Zhao, J. B.; Cusido, J.; Raymo, F. M.; Yuan, J. L.; Yang, S.; Leif, R. C.; Huo, Y. J.; Piper, J. A.; Robinson, J. P.; Goldys, E. M.; Jin, D. Y. On-the-Fly Decoding of Luminescence Lifetimes in the Microsecond Region for Lanthanide-Encoded Suspension Arrays. *Nat. Commun.* **2014**, *5*, 3741.
(30) Lu, Y. Q.; Zhao, J. B.; Zhang, R.; Liu, Y. J.; Liu, D. M.; Goldys, E. M.; Yang, X. S.; Xi, P.; Sunna, A.; Lu, J.; Shi, Y.; Leif, R. C.; Huo, Y. J.; Shen, J.; Piper, J. A.; Robinson, J. P.; Jin, D. Y. Tunable Lifetime Multiplexing Using Luminescent Nanocrystals. *Nat. Photonics* **2014**, *8*, 32−37.
(31) Qiu, X.; Guo, J. J.; Jin, Z. W.; Petreto, A.; Medintz, I. L.; Hildebrandt, N. Multiplexed Nucleic Acid Hybridization Assays Using Single-FRET-Pair Distance-Tuning. *Small* **2017**, *13*, 1700332.
(32) Chen, C.; Ao, L.; Wu, Y.-T.; Cifliku, V.; Cardoso Dos Santos, M.; Bourrier, E.; Delbianco, M.; Parker, D.; Zwier, J. M.; Huang, L.; Hildebrandt, N. Single-Nanoparticle Cell Barcoding by Tunable FRET from Lanthanides to Quantum Dots. *Angew. Chem., Int. Ed.* **2018**, *57*, 13686−13690.
(33) Zhang, L.; Chen, C.; Li, W. J.; Gao, G. H.; Gong, P.; Cai, L. T. Living Cell Multilifetime Encoding Based on Lifetime-Tunable Lattice Strained Quantum Dots. *ACS Appl. Mater. Interfaces* **2016**, *8*, 13187−13191.
(34) Chen, C.; Zhang, P. F.; Gao, G. H.; Gao, D. Y.; Yang, Y.; Liu, H.; Wang, Y. H.; Gong, P.; Cai, L. T. Near-Infrared-Emitting Two-Dimensional Codes Based on Lattice-Strained Core/(Doped) Shell Quantum Dots with Long Fluorescence Lifetime. *Adv. Mater.* **2014**, *26*, 6313−6317.
(35) Qiu, X.; Guo, J. J.; Xu, J. Y.; Hildebrandt, N. Three-Dimensional FRET Multiplexing for DNA Quantification with Attomolar Detection Limits. *J. Phys. Chem. Lett.* **2018**, *9*, 4379−4384.
(36) Lakowicz, J. R. *Principles of Fluorescence Spectroscopy*, 3rd ed.; Springer: New York, 2006.
(37) *FRET - Förster Resonance Energy Transfer. From Theory to Applications*; Medintz, I. L., Hildebrandt, N., Eds.; Wiley-VCH: Weinheim, Germany, 2014; pp 105−164.
(38) Boeneman-Gemmill, K.; Diaz, S. A.; Blanco-Canosa, J. B.; Deschamps, J. R.; Pons, T.; Liu, H. W.; Deniz, A.; Melinger, J.; Oh, E.; Susumu, K.; Stewart, M. H.; Hastman, D. A.; North, S. H.; Delehanty, J. B.; Dawson, P. E.; Medintz, I. L. Examining the Polyproline Nanoscopic Ruler in the Context of Quantum Dots. *Chem. Mater.* **2015**, *27*, 6222−6237.
(39) Xu, J.; Corneillie, T. M.; Moore, E. G.; Law, G.-L.; Butlin, N. G.; Raymond, K. N. Octadentate Cages of Tb(III) 2-Hydroxyisophthalamides: A New Standard for Luminescent Lanthanide Labels. *J. Am. Chem. Soc.* **2011**, *133*, 19900−19910.
(40) Hess, K. L.; Oh, E.; Tostanoski, L. H.; Andorko, J. I.; Susumu, K.; Deschamps, J. R.; Medintz, I. L.; Jewell, C. M.: Engineering Immunological Tolerance Using Quantum Dots to Tune the Density of Self-Antigen Display. *Adv. Funct. Mater.* **2017**, *27*. DOI: 10.1002/adfm.201770132
(41) Breger, J. C.; Muttenthaler, M.; Delehanty, J. B.; Thompson, D. A.; Oh, E.; Susumu, K.; Deschamps, J. R.; Anderson, G. P.; Field, L. D.; Walper, S. A.; Dawson, P. E.; Medintz, I. L. Nanoparticle Cellular Uptake by Dendritic Wedge Peptides: Achieving Single Peptide Facilitated Delivery. *Nanoscale* **2017**, *9*, 10447−10464.
(42) Mei, B. C.; Susumu, K.; Medintz, I. L.; Delehanty, J. B.; Mountziaris, T. J.; Mattoussi, H. Modular poly(ethylene glycol) ligands for biocompatible semiconductor and gold nanocrystals with extended pH and ionic stability. *J. Mater. Chem.* **2008**, *18*, 4949−4958.
(43) Mei, B. C.; Susumu, K.; Medintz, I. L.; Mattoussi, H. Polyethylene Glycol-Based Bidentate Ligands to Enhance Quantum Dot and Gold Nanoparticle Stability in Biological Media. *Nat. Protoc.* **2009**, *4*, 412−423.
(44) Diaz, S. A.; Sen, S.; Gemmill, K. B.; Brown, C. W.; Oh, E.; Susumu, K.; Stewart, M. H.; Breger, J. C.; Aragones, G. L.; Field, L. D.; Deschamps, J. R.; Kral, P.; Medintz, I. L. Elucidating Surface Ligand-Dependent Kinetic Enhancement of Proteolytic Activity at Surface-Modified Quantum Dots. *ACS Nano* **2017**, *11*, 5884−5896.
(45) Boeneman Gemmill, K.; Deschamps, J. R.; Delehanty, J. B.; Susumu, K.; Stewart, M. H.; Glaven, R. H.; Anderson, G. P.; Goldman, E. R.; Huston, A. L.; Medintz, I. L. Optimizing Protein Coordination to Quantum Dots with Designer Peptidyl Linkers. *Bioconjugate Chem.* **2013**, *24*, 269−281.
(46) Hildebrandt, N.; Wegner, K. D.; Algar, W. R. Luminescent terbium complexes: Superior Förster Resonance Energy Transfer Donors for Flexible and Sensitive Multiplexed Biosensing. *Coord. Chem. Rev.* **2014**, *273*, 125−138.
(47) Wu, Y.-T.; Qiu, X.; Lindbo, S.; Susumu, K.; Medintz, I. L.; Hober, S.; Hildebrandt, N. Quantum Dot−Based FRET Immunoassay for HER2 Using Ultrasmall Affinity Proteins. *Small* **2018**, *14*, 1802266.
(48) Algar, W. R.; Ancona, M. G.; Malanoski, A. P.; Susumu, K.; Medintz, I. L. Assembly of a Concentric Förster Resonance Energy Transfer Relay on a Quantum Dot Scaffold: Characterization and Application to Multiplexed Protease Sensing. *ACS Nano* **2012**, *6*, 11044−11058.
(49) Prasuhn, D. E.; Deschamps, J. R.; Susumu, K.; Stewart, M. H.; Boeneman, K.; Blanco-Canosa, J. B.; Dawson, P. E.; Medintz, I. L. Polyvalent Display and Packing of Peptides and Proteins on Semiconductor Quantum Dots: Predicted Versus Experimental Results. *Small* **2010**, *6*, 555−564.
(50) Wegner, K. D.; Morgner, F.; Oh, E.; Goswami, R.; Susumu, K.; Stewart, M. H.; Medintz, I. L.; Hildebrandt, N. Three-Dimensional Solution-Phase Förster Resonance Energy Transfer Analysis of Nanomolar Quantum Dot Bioconjugates with Subnanometer Resolution. *Chem. Mater.* **2014**, *26*, 4299−4312.
(51) Murphy, M. C.; Rasnik, I.; Cheng, W.; Lohman, T. M.; Ha, T. J. Probing Single-Stranded DNA Conformational Flexibility Using Fluorescence Spectroscopy. *Biophys. J.* **2004**, *86*, 2530−2537.
(52) Geissler, D.; Charbonniere, L. J.; Ziessel, R. F.; Butlin, N. G.; Löhmannsröben, H. G.; Hildebrandt, N. Quantum Dot Biosensors for Ultrasensitive Multiplexed Diagnostics. *Angew. Chem., Int. Ed.* **2010**, *49*, 1396−1401.
(53) Stround, J. http://structure.usc.edu/make-na/. 2013 (Access date: 05/11/2018).

DOI: 10.1021/acsnano.8b07137
ACS Nano 2019, 13, 505−514

(54) Macke, T.; Case, D. A. Modeling Unusual Nucleic Acid Structures. In *Molecular Modeling of Nucleic Acids*; Leontes, N. B., SantaLucia, J., Jr., Eds.; American Chemical Society: Washington, DC, 1998; pp 379−393.
(55) Macke, T.; Svrcek-Seiler, W. A.; Brown, R. A.; Kolossvary, I.; Bomble, Y.; Case, D. A. Generation of Models for "Unusual" DNA and RNA: A Computer Language for Structural Exploration. http://casegroup.rutgers.edu/casegr-sh-2.2.html. 2018 (Access date: 05/11/2018).
(56) Smith, S. B.; Cui, Y. J.; Bustamante, C. Overstretching B-DNA: The Elastic Response of Individual Double-Stranded and Single-Stranded DNA Molecules. *Science* **1996**, *271*, 795−799.
(57) Zhang, Y.; Zhou, H. J.; Ou-Yang, Z. C. Stretching Single-Stranded DNA: Interplay of Electrostatic, Base-Pairing, and Base-Pair Stacking Interactions. *Biophys. J.* **2001**, *81*, 1133−1143.
(58) Pettersen, E. F.; Goddard, T. D.; Huang, C. C.; Couch, G. S.; Greenblatt, D. M.; Meng, E. C.; Ferrin, T. E. UCSF Chimera - A Visualization System for Exploratory Research and Analysis. *J. Comput. Chem.* **2004**, *25*, 1605−1612.
(59) Wang, J. M.; Wang, W.; Kollman, P. A.; Case, D. A. Automatic Atom Type and Bond Type Perception in Molecular Mechanical Calculations. *J. Mol. Graphics Modell.* **2006**, *25*, 247−260.

DOI: 10.1021/acsnano.8b07137
ACS Nano 2019, 13, 505−514